Zhang, Y., Wang, R., Walter, T. R., Feng, W., Chen, Y., Huang, Q. (2017): Significant lateral dip changes may have limited the scale of the 2015 Mw7.8 Gorkha earthquake. - *Geophysical Research Letters*, *44*, 17, pp. 8847—8856.

DOI: http://doi.org/10.1002/2017GL074095

AGU PUBLICATIONS

Geophysical Research Letters

RESEARCH LETTER
10.1002/2017GL074095

Key Points:
- The two-dimensional dip variation of the 2015 Gorkha earthquake was estimated
- A lateral large-dip anomaly was found in the northeast corner of the rupture area, which may be associated with the slab tearing
- The large-dip anomaly limits the earthquake scale by blocking the east-southeastward propagations of deep ruptures

Supporting Information:
- Supporting Information S1

Correspondence to:
Y. Zhang,
zhygn@163.com

Citation:
Zhang, Y., R. Wang, T. R. Walter, W. Feng, Y. Chen, and Q. Huang (2017), Significant lateral dip changes may have limited the scale of the 2015 M_w 7.8 Gorkha earthquake, *Geophys. Res. Lett.*, *44*, 8847–8856, doi:10.1002/2017GL074095.

Received 10 MAY 2017
Accepted 23 AUG 2017
Accepted article online 29 AUG 2017
Published online 12 SEP 2017

Significant lateral dip changes may have limited the scale of the 2015 M_w 7.8 Gorkha earthquake

Yong Zhang[1], Rongjiang Wang[2], Thomas R. Walter[2], Wanpeng Feng[3], Yongshun Chen[1], and Qinghua Huang[1]

[1]School of Earth and Space Sciences, Peking University, Beijing, China, [2]Helmholtz Centre Potsdam, GFZ German Research Centre for Geosciences, Potsdam, Germany, [3]Canada Center for Mapping and Earth Observations, Natural Resources Canada, Ottawa, Ontario, Canada

Abstract The 2015 M_w 7.8 Gorkha earthquake has drawn interest due to its complex fault geometry. Both geodetic and geologic studies have focused on the dip variations. In this study we invert the coseismic geodetic data for the 2-D dip variations of the earthquake. The best fit model confirms that the dip varies with depth, and suggests that there is a significant lateral dip anomaly along strike. The depth-dependent dip variation suggests that the earthquake ruptured a ramp-flat fault. The shallow ramp may have prevented the rupture breaking through the surface. In addition, a lateral large-dip anomaly is found in the northeastern corner of the slip area, which supports the previous findings of inferred interseismic fault coupling, coseismic high-frequency radiations, and the aftershock mechanisms. This lateral dip anomaly is likely associated with local tearing within the Indian slab. It may have blocked the east-southeastward rupture propagations of the Gorkha earthquake, implying important controls on the earthquake scale and the spatial limits of ruptures.

1. Introduction

Seismicity, slip pattern, and residual stress are strongly affected by fault bends and segmentations [*Segall and Pollard*, 1980; *Ben-Zion and Rice*, 1995; *Saucier et al.*, 1992]. For thrust faults, on which most great earthquakes and tsunami disasters are generated, the dip can be quite variable [*Suppe*, 1983; *Suppe and Medwedeff*, 1990; *Hayes et al.*, 2012]. Since the variation in dip exerts a strong control on the seismogenic environment and earthquake processes [*Jordán et al.*, 1983; *Pardo and Suárez*, 1995; *Duputel et al.*, 2016; *Elliott et al.*, 2016], a detailed description of the fault dip would be helpful in increasing our understanding of the source physics and disaster-causing mechanism. A region exceptionally well suited for the analysis of fault dip variations is the collision zone between the Eurasian and Indian plates. The collision of the two plates resulted in the seismically active Main Himalayan Thrust (MHT) [*Bilham*, 2004]. According to current knowledge, the MHT branches into several steep faults in the upper crust (<5 km) and exhibits a ramp in the middle crust [*Pandey et al.*, 1995; *Avouac*, 2003; *Elliott et al.*, 2016], indicating a variable ramp-flat-ramp geometry. Moreover, it has been found that the underthrusting angle of the Indian slab varies from west to east [*Zhao et al.*, 2010]; that is, the dip of the MHT changes laterally. This lateral dip variation is consistent with the discontinuity in the interseismic seismicity around Nepal [*Pandey et al.*, 1999], from which the MHT is supposed to be segmented along strike. Although some efforts have been made to distinguish the geometric shape of the MHT [e.g., *Zhao et al.*, 1993; *Lemonnier et al.*, 1999; *Duputel et al.*, 2016], the detailed 2-D dip variation was not very well determined until the occurrence of the 2015 Gorkha earthquake.

The 25 April 2015 M_w 7.8 Gorkha earthquake was the largest earthquake that occurred on the MHT in the past 50 years. The earthquake was well recorded by modern geodetic measurements [*Galetzka et al.*, 2015; *Feng et al.*, 2016], providing us with an unprecedented opportunity to investigate the variations in dip. The overall fault dip is estimated to be approximately 6–11° based on seismic and geodetic analyses [*Avouac et al.*, 2015; *Diao et al.*, 2015; *Hayes et al.*, 2015; *Liu and Ge*, 2015; *Shan et al.*, 2015; *Wang and Fialko*, 2015; *Wang et al.*, 2015; *Zhang and Xu*, 2015; *Zhang et al.*, 2015; *Liu et al.*, 2016], suggesting that the earthquake mainly ruptured a flat portion of the MHT. Some geodetic analyses found that a listric fault could explain the surface deformations better than a planar fault could [*Wang and Fialko*, 2015; *Elliott et al.*, 2016], implying that ruptures may have reached the shallow steep fault branches. Although interseismic GPS and leveling data support a midcrustal ramp located at a depth of greater than 15 km, coseismic geodetic modeling did not find that the ramp

ruptured during the Gorkha event [*Elliott et al.*, 2016]. Lateral changes in the fault geometry may also exist in the earthquake rupture area, which is supported by the fact that two fault segments have been identified based on their significantly different seismicity at approximately 85.0°E [*Pandey et al.*, 1999]. This fault segmentation has been confirmed by *Whipple et al.* [2016], who performed a two-step inversion and found a steep fault segment in the eastern corner of the rupture area; that is, the dip may change laterally. Previous geodetic studies focused on either the depth-dependent dip variation [*Wang and Fialko*, 2015; *Elliott et al.*, 2016], or the lateral dip change [*Whipple et al.*, 2016]. There has been no a complete 2-D geodetic dip model. In addition, a geological study has constructed a fault model of the MHT around Nepal [*Hubbard et al.*, 2016], providing a completely independent dip estimation. Comparisons between the fault model and the slip distributions suggests that the Gorkha earthquake mainly ruptured a flat area that is surrounded by steeper ramps [*Hubbard et al.*, 2016], indicating that the dip is closely correlated with the slip distribution. In this work, we will introduce a new geodetic inversion method to investigate the 2-D dip variations and to further clarify the slip-dip correlations of the earthquake.

2. Methods

In contrast to the conventional geodetic inversion scheme, which estimates fault geometric parameters using a nonlinear method [*Wright et al.*, 1999; *Feng et al.*, 2010], in this work, we determine the dip variations by solving for the seismic moment tensors of the subfaults. A similar method was introduced by *Zhang and Wang* [2015], which estimated the deviatoric moment tensors (DMTs) of the subfaults and determined the along-strike variations of the strike, dip, rake, and moment of the 2008 M_w 7.9 Wenchuan earthquake. The basic rationale of this work is that for a thrust mechanism (rake = 90°) point source with a given strike φ and a varied dip δ, the moment tensor is linearly represented by two elementary double-couple moment tensors of strike = φ, dip = 0°, and rake = 90° and strike = φ, dip = 45°, and rake = 90°. In this case, the dip angle can be estimated by solving a linear equation.

Taking the coordinate system (x = north, y = east, z = down) with the source as the origin, the seismic moment tensor elements of a point double-couple source are as follows [*Aki and Richards*, 1980]:

$$\begin{cases} M_{xx} = -M_0\left(\sin\delta\ \cos\lambda\ \sin2\varphi + \sin2\delta\ \sin\lambda\ \sin^2\varphi\right) \\ M_{xy} = +M_0\left(\sin\delta\ \cos\lambda\ \cos2\varphi + \frac{1}{2}\sin2\delta\ \sin\lambda\ \sin2\varphi\right) = M_{yx} \\ M_{xz} = -M_0\left(\cos\delta\ \cos\lambda\ \cos\varphi + \cos2\delta\ \sin\lambda\ \sin\varphi\right) = M_{zx} \\ M_{yy} = +M_0\left(\sin\delta\ \cos\lambda\ \sin2\varphi - \sin2\delta\ \sin\lambda\ \cos^2\varphi\right) \\ M_{yz} = -M_0\left(\cos\delta\ \cos\lambda\ \sin\varphi - \cos2\delta\ \sin\lambda\ \cos\varphi\right) = M_{zy} \\ M_{zz} = +M_0\ \sin2\delta\ \sin\lambda, \end{cases} \tag{1}$$

where M_0 is the scalar moment and φ, δ, and λ are the strike, dip, and rake, respectively. Items containing $\cos\lambda$ and $\sin\lambda$ in equation (1) correspond to the strike slip and dip slip, respectively. For a thrust faulting earthquake ($\lambda = 90°$) with a known or assumed strike (φ) and a variable dip (δ), the moment tensor is $M = M^D = \alpha M_0^D + \beta M_{45}^D$, where α and β equal $M_0 \cos 2\delta$ and $M_0 \sin 2\delta$, respectively. M_0^D and M_{45}^D are two elementary moment tensors,

$$\begin{aligned} M_0^D &= M^D(\delta = 0°) = \begin{bmatrix} 0 & 0 & -\sin\varphi \\ 0 & 0 & \cos\varphi \\ -\sin\varphi & \cos\varphi & 0 \end{bmatrix}, \\ M_{45}^D &= M^D(\delta = 45°) = \begin{bmatrix} -\sin^2\varphi & \frac{1}{2}\sin2\varphi & 0 \\ \frac{1}{2}\sin2\varphi & -\cos^2\varphi & 0 \\ 0 & 0 & 1 \end{bmatrix}. \end{aligned} \tag{2}$$

If α and β are both positive, the dip would be confined between 0° and 45° by $\delta=\frac{1}{2}\arctan\left(\frac{\beta}{\alpha}\right)$, and the scalar moment $M_0=\sqrt{\alpha^2+\beta^2}$. The slip can be obtained by $d=\frac{M_0}{\mu A}$, where μ and A are the shear modulus and the area of subfault, respectively.

By discretizing the finite fault into subfaults, which are represented as point sources [*Zhang and Wang*, 2015], we can estimate the dips of all of the subfaults by minimizing the following function:

$$\Delta=\left\|u-\sum_{k=1}^{N}\left(g_{0k}^{D}\alpha_k+g_{45k}^{D}\beta_k\right)\right\|_2+\kappa\left\|\nabla^2\alpha\right\|_2+\kappa\left\|\nabla^2\beta\right\|_2, \tag{3}$$

where N is the number of subfaults, u is the surface deformation, g_0^D and g_{45}^D are the Green's functions of the two elementary mechanisms M_0^D and M_{45}^D, respectively, and κ is the weight of the spatial Laplacian smoothing. By assuming X_A and X_B are vectors containing unknowns α and β, equation (3) can be rewritten as follows:

$$\begin{bmatrix} G_0^D & G_{45}^D \\ \kappa D & 0 \\ 0 & \kappa D \end{bmatrix}\begin{bmatrix} X_A \\ X_B \end{bmatrix}=\begin{bmatrix} u \\ 0 \\ 0 \end{bmatrix}, \tag{4}$$

where D is the matrix of smoothing. When a proper smoothing factor is applied, we can get the slip and dip angles of all of the subfaults by solving equation (4). In this study, the Green's functions were calculated based on the elastic dislocation theory [*Okada*, 1985]. A nonnegative gradient method [*Ward and Barrientos*, 1986] was used to solve equation (4) to retrieve a dip variation between 0° and 45°.

The dip variation inversion is generally performed on a given planar fault. In this case, the depth of the subfault point sources would be different from the real sources if a curved fault was ruptured. To determine how the depth difference biases the dip estimates, we performed a series of tests for a point source with different dips and depths (Figure S1). When the depth assumed in the inversion (d_i) is shallower than the real depth (d_r), the dip would be underestimated; otherwise, it would lead to overestimation. Although the underestimates and overestimates are not significant (<6° when $0.5<d_i/d_r<2$), there are some trade-offs between the depth and dip. To minimize these trade-offs, we optimize the position and orientation of the planar fault through a grid search. Based on a synthetic test (Figure S2), we confirm that this practice can successfully recover the major dip features.

3. Data Weighting and Dip Variation Inversion

In application to the 2015 Gorkha earthquake, we inverted the coseismic interferometric synthetic aperture radar (InSAR) and Global Positioning System (GPS) displacements to determine the dip variations. The InSAR coseismic measurements used in this study were compiled by *Feng et al*. [2016] and include six coseismic interferograms for the 2015 Gorkha earthquake from various satellites, including ALOS-2, Sentinel-1A, and RADARSAT-2. In total, one ascending and five descending tracks were corrected for potential orbital and ionospheric errors using the coseismic GPS data. Among them, ScanSAR track 048 from ALOS-2 covers the entire epicentral area, providing excellent spatial coverage of the coseismic surface deformation field of the earthquake [*Lindsey et al.*, 2015].

The coseismic GPS data from 13 stations were released by University NAVSTAR Consortium (UNAVCO). Five stations located between 85.1 and 85.3°E show horizontal displacements exceeding 0.5 m [Figure 1]. Other stations were also used in the inversion, but they are not sensitive to the dip variation due to being far away from the source. Since the GPS data with significant deformation covered only about a quarter of the deformation area along strike, its relative weight compared with the InSAR data was set to be 0.25.

A 185 km long and 100 km wide planar fault, which was equally divided into subfaults with areas of 5 km by 5 km, was assumed for the inversion. Through a 3-D (position, overall strike, and overall dip) grid search, the position and orientation of the planar fault were optimized (Figure S3). An overall dip of 10° was found to lead to a minimum misfit. We also tried other overall dips (6° and 16°) and found that

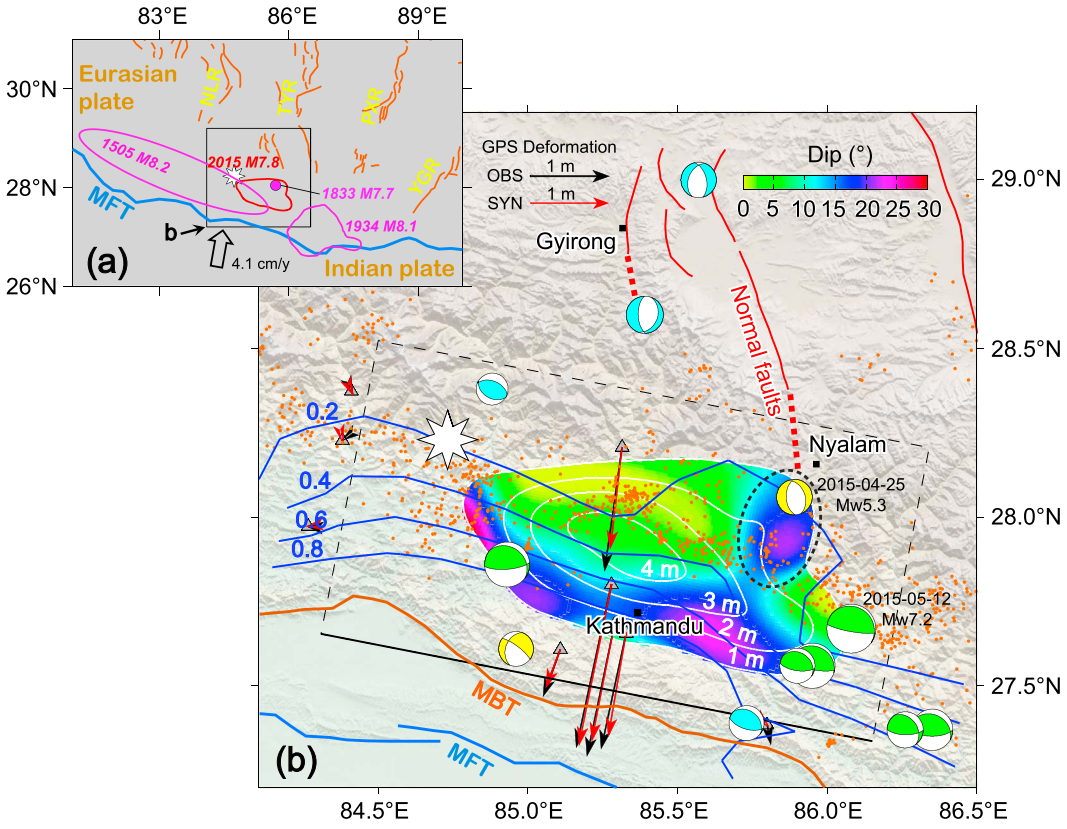

Figure 1. (a) Regional tectonics near the epicentral area of the 2015 Gorkha earthquake. The main frontal thrust (MFT), the rupture areas of significant earthquakes, and the N-S trending rifts in southern Tibet are plotted [*Deng et al.*, 2003] (NLR: northern Lunggar rift, TYR: Tangra Yum Co rift, PXR: Pumqu-Xianza rift, YGR: Yadong-Gulu rift). (b) Surface projections of the dip variation and slip distribution determined in this study (white contour lines). The star denotes the epicenter. Beach balls are mechanism solutions of historic earthquakes (cyan balls) and aftershocks (green and yellow balls) released by the Global Centroid Moment Tensor (GCMT) group. Blue isolines are long-term interseismic couplings [*Stevens and Avouac*, 2015]. Orange dots represent the interseismic seismicity [*Ader et al.*, 2012]. The dashed black ellipse marks the large-dip anomaly. Full red lines are the N-S trending normal faults [*Deng et al.*, 2003], and the dashed red lines are deduced fault tracks. Black and red arrows are observed and modeled GPS displacements, respectively.

they led to similar dip features (Figure 2). This confirms that the geometric shape of the fault does not strongly impact the dip variation estimates. After optimization of the fault position and orientation, we discretized the fault plane into subfaults of 1 km by 1 km to achieve a higher spatial resolution (Figure 1). The final model was determined by balancing data fitting and slip roughness (Figures S4 and S5).

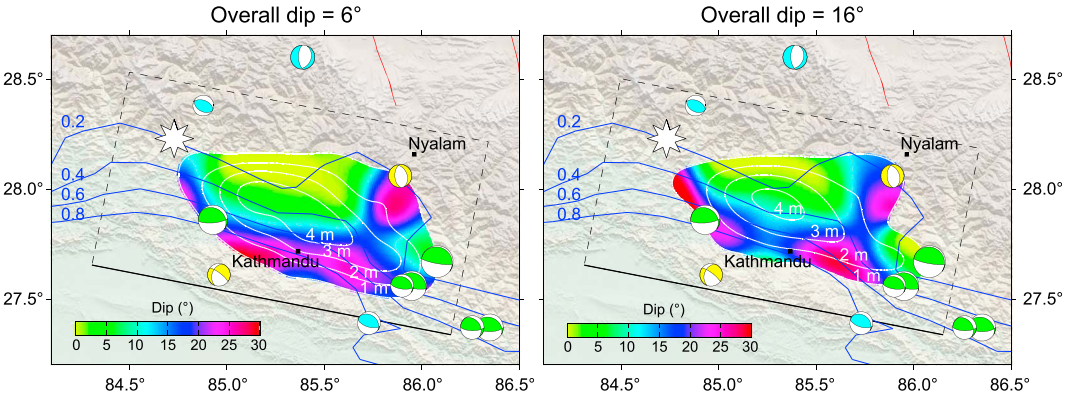

Figure 2. Dip models determined using different overall fault dips of (left) 6° and (right) 16°.

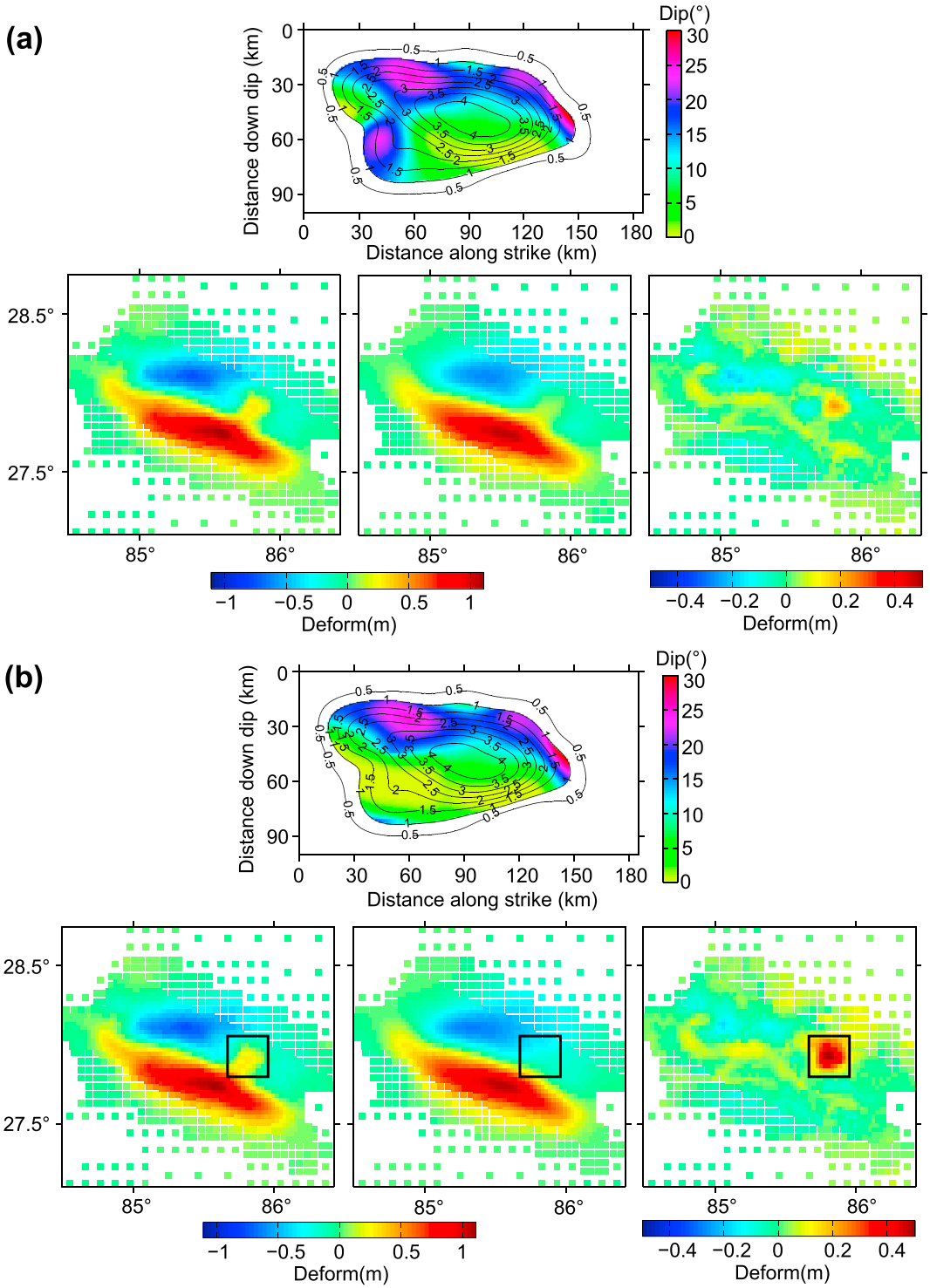

Figure 3. (a) The top panel is the obtained dip model. From left to right, the bottom three panels are the observed InSAR data for scanSAR track 048, the predicted InSAR data, and the residuals. (b) Panels are the same as in Figure 3a, but the dip anomaly has been modified to be consistent with the surrounding areas. Black rectangles in Figure 3b outline the area where the uplift deformation caused by the dip anomaly is poorly fitted.

4. Results

The obtained dip variation is shown in Figure 1. The earthquake ruptured a fault with a length and width of approximately 150 km and 60 km, respectively. The dip significantly decreases from 30° in the south to approximately 0° in the north, which is basically consistent with other geodetic 1-D dip models [*Wang and Fialko*, 2015; *Elliott et al.*, 2016]. In the north, although a midcrustal ramp was widely hypothesized to exist, it was not found in this work or in other coseismic geodetic inversions [*Wang and Fialko*, 2015; *Elliott et al.*, 2016]. Two reasons may account for this. First, as *Elliott et al.* [2016] have suggested, the surface deformation inversions have a relatively poor resolution at depth. Second, the northern ramp is weakly locked. The strain has been released by small events or by creeping during the interseismic period [*Pandey et al.*, 1995; *Elliott et al.*, 2016], resulting in failure of the ramp to rupture during the main shock. The southernmost dips are about 30°, consistent with the existing geodetic inversions [*Wang and Fialko*, 2015; *Elliott et al.*, 2016] and geologic results [*Hubbard et al.*, 2016]. This shallow ramp may have blocked the ruptures and could account for the fact that the rupture did not break through the surface. Both the dip and slip distributions (see Figure 1) reveal that a portion of the main boundary thrust (MBT) may have ruptured. It is clear that the dip angles (with slip >1 m; Figure 1) decrease with increasing distance from the MBT. In addition, the southernmost slip isoclines (slip = 1 m) are nearly parallel to the MBT trace. It should be noted that other geodetic slip models also exhibit this feature [*Wang and Fialko*, 2015; *Elliott et al.*, 2016; *Feng et al.*, 2016]. Hence, the shallow ruptures of the 2015 main shock are likely controlled by the MBT, rather than by the main frontal thrust (MFT).

The dip variations can successfully explain the interseismic fault couplings and the historic microseismicity. For a thrust fault, in principle, large dips lead to large normal stresses, and thus, they correspond to high interseismic fault couplings [*Scholz and Small*, 1997]. This can be demonstrated in the comparison between dip variations and fault couplings [*Stevens and Avouac*, 2015] (Figure 1). A steep fault segment (with a large dip) at a shallow depth is more locked, while a flat segment (with a small dip) at a greater depth is less locked (Figure 1).

In addition to the depth-dependent change, the dip also demonstrates a significant lateral variation. In particular, a large-dip ($>15°$) anomaly appears in the northeastern corner of the rupture area (slip >1 m, Figure 1b), where the fault coupling level of 0.2 extends over a broad area to the north. This is consistent with the study of *Whipple et al.* [2016], who concluded that a steep fault segment is required in the eastern part of the slip area to explain the observed surface deformation, and with the geological result of *Hubbard et al.* [2016], in which the northeastern slips reached and ruptured a ramp. This dip anomaly spatially correlates to the surface uplift anomaly revealed by the InSAR data (outlined by rectangles in Figure 3). By modifying the dip anomaly to make it consistent with the surrounding area, the uplift deformations become poorly fitted, and the border between the uplift and subsidence areas becomes more regular (Figure 3). In this case, the abnormally uplifted area revealed by the InSAR data is actually caused by the large-dip anomaly at depth.

5. Discussion and Conclusions

In principle, the fault geometry is correlated with the aftershock locations. For the Gorkha earthquake, however, aftershocks do not suggest a clear geometric shape of the fault. Instead, most events are above the MHT [*Bai et al.*, 2016], making them difficult to use for rebuilding the fault geometry. Fortunately, high-quality geodetic data are available, offering us the opportunity to investigate the fault geometry of the earthquake.

The previous geodetic analysis estimated the dip features using trial-and-error methods [*Wang and Fialko*, 2015; *Elliott et al.*, 2016; *Whipple et al.*, 2016]. These methods are effective in determining the major dip features. In contrast, we estimate the dip variation by inverting the moment tensors of the subfaults. The specialty of our method is that the strike and rake are assumed and fixed, which reduces the number of unknowns and helps to improve the stability. Since our method is based on the point source approximation, i.e., the subfault size must be much smaller than the distance between the source and the observation, a large number of subfaults are generated and a large amount of calculation time is needed. Meanwhile, the advantage of the method is that it is independent of experience to a large extent, and thus, it can be applied to more general cases.

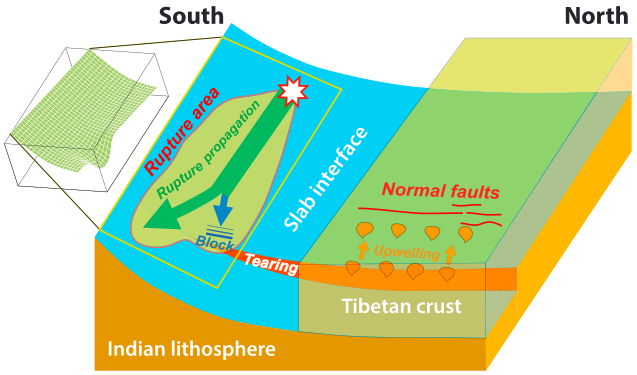

Figure 4. Schematic diagram of slab tearing. The slab tearing causes the hot asthenosphere to upwell, resulting in N-S trending normal faults. It also leads to the large-dip anomaly, which blocked the rupture propagations of the Gorkha earthquake. The inset in the top-left corner illustrates the inferred fault geometry with the determined 2-D dip variations.

The final estimated 2-D dip model (shown in Figure 1b) is consistent with previous studies. It successfully confirms not only the depth-dependent dip variation [*Wang and Fialko*, 2015; *Elliott et al.*, 2016] but also the change in the lateral dip [*Whipple et al.*, 2016]. Significant slips are mainly distributed in areas with gentle dips, which support the geologic results that the slip is mainly distributed on a flat portion of the fault [*Hubbard et al.*, 2016].

It should be noted that other geodetic slip inversions, based on uniform dip angles (without the shallow ramp and the lateral large-dip anomaly), also lead to equally good data fits [e.g., *Feng et al.*, 2016]. This is because for a low-angle thrust fault, the uplift deformation can be explained by either large slips on a flat fault (small dip), or small slips on a steep fault (large dip), that is, the trade-off between slips and dips. To check whether dip variation is necessary to explain the data, we performed a series of rake variation inversions (i.e., the conventional slip inversion in which the rake can be variable but the dip is fixed) and deviatoric moment tensor (DMT) variation inversions [*Zhang and Wang*, 2015] with different smoothing factors. Comparisons of the roughness-misfit curves of the dip, rake, and DMT inversions reveal useable information about the fault (Figure S6). When the smoothing strength in the inversion is weak (i.e., large roughness), the DMT inversions, which have more unknowns, have smaller misfits to those of the dip and rake inversions. If strong smoothing is considered (small roughness), the misfits of the dip and DMT inversions are almost identical and are both significantly less than those of the rake inversions. This indicates that the observations can be equally explained by either variable dips or variable DMTs if a reasonably smooth solution is required. The strike, dip, and rake derived from the DMT inversion are shown in Figure S7. Because of the low dip angle, the strike and rake are coupled together, which makes them difficult to determine. However, the movement direction of the hanging wall relative to the footwall (strike minus rake) is successfully calculated (see Figure S7e). The average direction of the hanging wall movement is about 189°, which is consistent with the moment tensor solutions of the GCMT group and the United States Geological Survey. In addition, in the DMT variation model, there are some unreasonable negative dips at depth. These negative dips are caused by the uncertainties involved in solving a large number of unknowns in the DMT inversion. Even so, it clearly suggests that the dip is the most variable fault parameter (Figure S7 and S8); i.e., the dip variation is necessary to explain the data. Similar to the dip variation model (Figure 1b), the DMT model also exhibits the shallow ramp and the lateral large-dip anomaly (Figure S7b and S7d). This agreement between the dip and DMT models demonstrates that the dip model determined in this work is highly reliable.

Existing seismic evidence supports the fact that the cause of the large-dip anomaly may be related to fragmentation or tearing of the Indian slab. Seismic tomographic studies have found low velocity zones around the N-S trending rifts (Figure 1a) from central to southern Tibet [*Liang et al.*, 2011; *Xu et al.*, 2011; *Liang et al.*, 2012; *Pei et al.*, 2016]. The existence of these low velocity zones are supported by the presence of lateral differences in the delay time in the SKS wave splitting measurements [*Chen et al.*, 2015]. A possible interpretation of these lateral variations in the velocity structure is tearing within the Indian slab [*Liang et al.*, 2011; *Xu et al.*, 2011; *Liang et al.*, 2012; *Chen et al.*, 2015; *Pei et al.*, 2016]. When this tearing reaches the slab interface in the south, it would change the geometry of the MHT and result in a large-dip anomaly (Figure 4). On the other hand, this slab tearing provides a passage for asthenospheric upwelling and leads to the N-S trending rifts and normal faults observed in central and southern Tibet [*Liang et al.*, 2012] (Figure 4). A normal fault of the Tangra Yum Co Rift (TYR), which has not been fully traced, may extend to the south and reach the MHT near 85.8°E at Nyalam (Figure 1b). During the Gorkha earthquake, the east-southeast ruptures got

close to this fault, and triggered a M_w 5.3 normal fault aftershock 11 h after the Gorkha main shock (yellow beach ball in the dashed ellipse, Figure 1b).

This dip anomaly could play an important role in the earthquake rupture processes by stopping the east-southeastward propagation of deep ruptures. It has been confirmed that changes in fault geometry can behave as barriers and block rupture propagation [*Das*, 2007; *Bouchon and Karabulut*, 2008; *Zhang et al.*, 2014], which tend to generate high-frequency seismic waves [*Ben-Zion and Rice*, 1995]. A slip inversion of the Gorkha earthquake has revealed a large slip roughness and a long rise time in the northeastern corner of the slip area, around which the large-dip anomaly is located [*Yue et al.*, 2016]. This provides strong evidence that ruptures were blocked there. From back projection results, it has been found that a large part of the high-frequency radiations are located near the large-dip anomaly [*Zhang et al.*, 2016; *Yin et al.*, 2017]. These high-frequency radiations are probably the consequence of the rupture velocity being suddenly slowed down by the changes in fault geometry. This decrease in the rupture velocity also impacts the rupture extensions and causes different lateral dimensions of shallow and deep ruptures (Figure 1b). Compared with the deep ruptures, the shallow ruptures propagated farther to the east-southeast for 20–30 km. They triggered a series of thrust mechanism aftershocks, including the largest 12 May 2015 M_w 7.2 shock (Figure 1b). In contrast, the deep ruptures were blocked in the area around the dip anomaly (Figure 4). In this case, the large-dip anomaly limits the scale of the earthquake to some extent. Without this lateral dip variation, the deep ruptures of the Gorkha earthquake would have propagated further east, which could have resulted in a larger magnitude and a more serious disaster.

The dependence between fault geometry and rupture dimension has been observed in geologic and seismologic studies [*King and Nabelek*, 1985; *Zhang et al.*, 1991; *Sekiguchi et al.*, 2000]. However, since the detailed fault geometry was not well determined, this relationship was mainly qualitative. This study presents a real case study of a thrust event for which the rupture termination and the earthquake scale are controlled by changes in the fault geometry. Our study indicates that the fault geometry is a critical factor in the fault seismogenic pattern, which is significant for earthquake hazard assessment and damage prevention. Future work is necessary to explore the possible geometry-dependent rupture behaviors of other earthquakes and to widely examine how common it is for a change in the fault geometry to block rupture propagation and control the spatial limits of fault slip.

Acknowledgments
The ALOS data, Sentinel-1A data, and the RADARSAT-2 data were provided by the JAXA, the ESA, and the Canada Space Agency, respectively. The GPS data were released by UNAVCO. This work was supported by the National Natural Science Foundation of China (NSFC) (grant 41541035 and 41574035).

References

Ader, T., J. P. Avouac, J. Liu-Zeng, H. Lyon-Caen, L. Bollinger, J. Galetzka, and S. Rajaure (2012), Convergence rate across the Nepal Himalaya and interseismic coupling on the Main Himalayan Thrust: Implications for seismic hazard, *J. Geophys. Res.*, *117*, B04403, doi:10.1029/2011JB009071.

Aki, K., and P. G. Richards (1980), *Quantitative Seismology: Theory and Methods*, vol. 1, W. H. Freeman, New York.

Avouac, J. P. (2003), Mountain building, erosion, and the seismic cycle in the Nepal Himalaya, *Adv. Geophys.*, *46*, 1–80.

Avouac, J. P., L. Meng, S. Wei, T. Wang, and J. P. Ampuero (2015), Lower edge of locked Main Himalayan Thrust unzipped by the 2015 Gorkha earthquake, *Nat. Geosci.*, *8*, 708–711.

Bai, L., H. Liu, J. Ritsema, J. Mori, T. Zhang, Y. Ishikawa, and G. Li (2016), Faulting structure above the Main Himalayan Thrust as shown by relocated aftershocks of the 2015 M_w7. 8 Gorkha, Nepal, earthquake, *Geophys. Res. Lett.*, *43*, 637–642, doi:10.1002/2015GL066473.

Ben-Zion, Y., and J. R. Rice (1995), Slip patterns and earthquake populations along different classes of faults in elastic solids, *J. Geophys. Res.*, *100*(B7), 12,959–12,983, doi:10.1029/94JB03037.

Bilham, R. (2004), Earthquakes in India and the Himalaya: Tectonics, geodesy and history, *Ann. Geophys.*, *47*, 2–3.

Bouchon, M., and H. Karabulut (2008), The aftershock signature of supershear earthquakes, *Science*, *320*(5881), 1323–1325.

Chen, Y., W. Li, X. Yuan, J. Badal, and J. Teng (2015), Tearing of the Indian lithospheric slab beneath southern Tibet revealed by SKS-wave splitting measurements, *Earth Planet. Sci. Lett.*, *413*, 13–24.

Das, S. (2007), The need to study speed, *Science*, *317*(5840), 905–906.

Deng, Q., P. Zhang, Y. Ran, X. Yang, W. Min, and Q. Chu (2003), Basic characteristics of active tectonics of China, *Sci. China, Ser. D Earth Sci.*, *46*(4), 356–372.

Diao, F., T. R. Walter, M. Motagh, P. Prats-Iraola, R. Wang, and S. V. Samsonov (2015), The 2015 Gorkha earthquake investigated from radar satellites: Slip and stress modeling along the MHT, *Front. Earth Sci.*, *3*, 65.

Duputel, Z., J. Vergne, L. Rivera, G. Wittlinger, V. Farra, and G. Hetényi (2016), The 2015 Gorkha earthquake: A large event illuminating the Main Himalayan Thrust fault, *Geophys. Res. Lett.*, *43*, 2517–2525, doi:10.1002/2016GL068083.

Elliott, J. R., R. Jolivet, P. J. González, J. P. Avouac, J. Hollingsworth, M. P. Searle, and V. L. Stevens (2016), Himalayan megathrust geometry and relation to topography revealed by the Gorkha earthquake, *Nat. Geosci.*, *9*, 174–180.

Feng, W., E. Lindsey, S. Barbot, S. Samsonov, K. Dai, P. Li, and X. Xu (2016), Source characteristics of the 2015 M_W 7.8 Gorkha (Nepal) earthquake and its M_W7.2 aftershock from space geodesy, *Tectonophysics*, *712*, 747–758.

Feng, W. P., L. S. Xu, Z. H. Li, C. Li, and Z. Xu (2010), Fault parameters of the October 2008 Damxung M(w)6.3 earthquake from InSAR inversion and its tectonic implication, *Chin. J. Geophys.*, *53*, 1134–1142.

Galetzka, J., D. Melgar, J. F. Genrich, J. Geng, S. Owen, E. O. Lindsey, and B. N. Upreti (2015), Slip pulse and resonance of the Kathmandu basin during the 2015 Gorkha earthquake, Nepal, *Science*, *349*(6252), 1091–1095.

Hayes, G. P., D. J. Wald, and R. L. Johnson (2012), Slab1.0: A three-dimensional model of global subduction zone geometries, *J. Geophys. Res.*, *117*, B01302, doi:10.1029/2011JB008524.
Hayes, G. P., R. W. Briggs, W. D. Barnhart, W. L. Yeck, D. E. McNamara, D. J. Wald, and K. Marano (2015), Rapid characterization of the 2015 M_w 7.8 Gorkha, nepal, earthquake sequence and its seismotectonic context, *Seismol. Res. Lett.*, *86*(6), 1557–1567.
Hubbard, J., R. Almeida, A. Foster, S. N. Sapkota, P. Bürgi, and P. Tapponnier (2016), Structural segmentation controlled the 2015 M_w 7.8 Gorkha earthquake rupture in Nepal, *Geology*, *44*(8), 639–642.
Jordán, T. E., B. L. Isacks, R. W. Allmendinger, J. A. Brewer, V. A. Ramos, and C. J. Ando (1983), Andean tectonics related to geometry of subducted Nazca plate, *Geol. Soc. Am. Bull.*, *94*(3), 341–361.
King, G., and J. Nabelek (1985), Role of fault bends in the initiation and termination of earthquake rupture, *Science*, *228*, 984–988.
Lemonnier, C., G. Marquis, F. Perrier, J. P. Avouac, G. Chitrakar, B. Kafle, and M. Bano (1999), Electrical structure of the Himalaya of Central Nepal: High conductivity around the mid-crustal ramp along the MHT, *Geophys. Res. Lett.*, *26*(21), 3261–3264, doi:10.1029/1999GL008363.
Liang, X., Y. Shen, Y. J. Chen, and Y. Ren (2011), Crustal and mantle velocity models of southern Tibet from finite frequency tomography, *J. Geophys. Res.*, *116*, B02408, doi:10.1029/2009JB007159.
Liang, X., E. Sandvol, Y. J. Chen, T. Hearn, J. Ni, S. Klemperer, and F. Tilmann (2012), A complex Tibetan upper mantle: A fragmented Indian slab and no south-verging subduction of Eurasian lithosphere, *Earth Planet. Sci. Lett.*, *333*, 101–111.
Lindsey, E. O., R. Natsuaki, X. Xu, M. Shimada, M. Hashimoto, D. Melgar, and D. T. Sandwell (2015), Line-of-sight displacement from ALOS-2 interferometry: M_w7.8 Gorkha earthquake and M_w 7.3 aftershock, *Geophys. Res. Lett.*, *42*, 6655–6661, doi:10.1002/2015GL065385.
Liu, C. L., Y. Zheng, R. Wang, B. Shan, Z. Xie, X. Xiong, and C. Ge (2016), Rupture processes of the 2015 Mw 7.9 Gorkha earthquake and its Mw7.3 aftershock and their implications on the seismic risk, *Tectonophysics*, *682*, 264–277.
Liu, Z. P., and Z. X. Ge (2015), Rupturing process of the MW7.9 Nepal earthquake inverted by the multi-array compressive sensing method, *Chin. J. Geophys.*, *58*(6), 1891–1899.
Okada, Y. (1985), Surface deformation due to shear and tensile faults in a half-space, *Bull. Seismol. Soc. Am.*, *75*(4), 1135–1154.
Pandey, M. R., R. P. Tandukar, J. P. Avouac, J. Lave, and J. P. Massot (1995), Interseismic strain accumulation on the Himalayan crustal ramp (Nepal), *Geophys. Res. Lett.*, *22*(7), 751–754, doi:10.1029/94GL02971.
Pandey, M. R., R. P. Tandukar, J. P. Avouac, J. Vergne, and T. Heritier (1999), Seismotectonics of the Nepal Himalaya from a local seismic network, *J. Asian Earth Sci.*, *17*(5), 703–712.
Pardo, M., and G. Suárez (1995), Shape of the subducted Rivera and Cocos plates in southern Mexico: Seismic and tectonic implications, *J. Geophys. Res.*, *100*(B7), 12,357–12,373, doi:10.1029/95JB00919.
Pei, S., H. Liu, L. Bai, Y. Liu, and Q. Sun (2016), High-resolution seismic tomography of the 2015 M_w7.8 Gorkha earthquake, Nepal: Evidence for the crustal tearing of the Himalayan rift, *Geophys. Res. Lett.*, *43*, 9045–9052, doi:10.1002/2016GL069808.
Saucier, F., E. Humphreys, and R. Weldon (1992), Stress near geometrically complex strike-slip faults: Application to the San Andreas fault at Cajon Pass, Southern California, *J. Geophys. Res.*, *97*(B4), 5081–5094, doi:10.1029/91JB02644.
Scholz, C. H., and C. Small (1997), The effect of seamount subduction on seismic coupling, *Geology*, *25*(6), 487–490.
Segall, P., and D. D. Pollard (1980), Mechanics of discontinuous faults, *J. Geophys. Res.*, *85*(B8), 4337–4350, doi:10.1029/JB085iB08p04337.
Sekiguchi, H., K. Irikura, and T. Iwata (2000), Fault geometry at the rupture termination of the 1995 Hyogo-ken Nanbu earthquake, *Bull. Seismol. Soc. Am.*, *90*(1), 117–133.
Shan, X. J., G. H. Zhang, C. S. Wang, et al. (2015), Joint inversion for the spatial fault slip distribution of the 2015 Nepal Mw7.9 earthquake based on InSAR and GPS observations, *Chin. J. Geophys.*, *58*(11), 4266–4276.
Stevens, V. L., and J. P. Avouac (2015), Interseismic coupling on the main Himalayan thrust, *Geophys. Res. Lett.*, *42*, 5828–5837, doi:10.1002/2015GL064845.
Suppe, J. (1983), Geometry and kinematics of fault-bend folding, *Am. J. Sci.*, *283*(7), 684–721.
Suppe, J., and D. A. Medwedeff (1990), Geometry and kinematics of fault-propagation folding, *Eclogae Geol. Helv.*, *83*(3), 409–454.
Wang, K., and Y. Fialko (2015), Slip model of the 2015 M_w 7.8 Gorkha (Nepal) earthquake from inversions of ALOS-2 and GPS data, *Geophys. Res. Lett.*, *42*, 7452–7458, doi:10.1002/2015GL065201.
Wang, W., J. Hao, J. He, and Z. Yao (2015), Rupture process of the Mw7.9 Nepal earthquake April 25, 2015, *Sci. China Earth Sci.*, *58*, 1895–1900.
Ward, S. N., and S. E. Barrientos (1986), An inversion for slip distribution and fault shape from geodetic observations of the 1983, Borah Peak, Idaho, earthquake, *J. Geophys. Res.*, *91*(B5), 4909–4919, doi:10.1029/JB091iB05p04909.
Whipple, K. X., M. Shirzaei, K. V. Hodges, and J. R. Arrowsmith (2016), Active shortening within the Himalayan orogenic wedge implied by the 2015 Gorkha earthquake, *Nat. Geosci.*, *9*, 711–716.
Wright, T. J. B., E. Parsons, J. A. Jackson, M. Haynes, E. J. Fielding, P. C. England, and P. J. Clarke (1999), Source parameters of the 1 October 1995 Dinar (Turkey) earthquake from SAR interferometry and seismic body wave modeling, *Earth Planet. Sci. Lett.*, *172*, 23–37.
Xu, Q., J. Zhao, S. Pei, and H. Liu (2011), The lithosphere-asthenosphere boundary revealed by *S*-receiver functions from the Hi-CLIMB experiment, *Geophys. J. Int.*, *187*(1), 414–420.
Yin, J., H. Yao, H. Yang, W. Qin, J. Liu-Zeng, and H. Zhang (2017), Frequency-dependent rupture process, stress change, and seismogenic mechanism of the 25 April 2015 Nepal Gorkha M_w7.8 earthquake, *Sci. China Earth Sci.*, *60*, 796.
Yue, H., M. Simons, Z. Duputel, J. Jiang, E. Fielding, C. Liang, and S. V. Samsonov (2016), Depth varying rupture properties during the 2015 Mw 7.8 Gorkha (Nepal) earthquake, *Tectonophysics*.
Zhang, H., S. Lee, and Z. Ge (2016), Multiarray rupture imaging of the devastating 2015 Gorkha, Nepal, earthquake sequence, *Geophys. Res. Lett.*, *43*, 584–591, doi:10.1002/2015GL066657.
Zhang, P., D. B. Slemmons, and F. Mao (1991), Geometric pattern, rupture termination and fault segmentation of the Dixie Valley—Pleasant Valley active normal fault system, Nevada, USA, *J. Struct. Geol.*, *13*(2), 165–176.
Zhang, X., and L. S. Xu (2015), Inversion of the apparent source time functions for the rupture process of the Nepal MS8.1 earthquake, *Chin. J. Geophys.*, *58*(6), 1881–1890.
Zhang, Y., and R. Wang (2015), Geodetic inversion for source mechanism variations with application to the 2008 Mw7.9 Wenchuan earthquake, *Geophys. J. Int.*, *200*(3), 1627–1635.
Zhang, Y., L. S. Xu, and Y. T. Chen (2015), Rupture process of the 2015 Nepal Mw7.9 earhquake: Fast inversion and preliminary joint inversion, *Chin. J. Geophys.*, *58*(5), 1804–1811.

Zhang, Z., W. Zhang, and X. Chen (2014), Three-dimensional curved grid finite-difference modelling for non-planar rupture dynamics, *Geophys. J. Int.*, *199*(2), 860–879.

Zhao, W., K. D. Nelson, J. Che, J. Quo, D. Lu, C. Wu, and X. Liu (1993), Deep seismic reflection evidence for continental underthrusting beneath southern Tibet, *Nature*, *366*(6455), 557–559.

Zhao, J., X. Yuan, H. Liu, P. Kumar, S. Pei, R. Kind, and Q. Xu (2010), The boundary between the Indian and Asian tectonic plates below Tibet, *Proc. Natl. Acad. Sci. U.S.A.*, *107*(25), 11,229–11,233.